# Test of methods to infer the magnetic reconnection geometry from spacecraft data

R. E. Denton,[1] B. U. Ö. Sonnerup,[2] J. Birn,[3] W.-L. Teh,[4] J. F. Drake,[5] M. Swisdak,[5] M. Hesse,[6] and W. Baumjohann[7]

Received 2 March 2010; revised 29 July 2010; accepted 4 August 2010; published 26 October 2010.

[1] When analyzing data from a cluster of spacecraft (such as Cluster or MMS) crossing a site of magnetic reconnection, it is desirable to be able to determine the orientation of the reconnection site. If the reconnection is quasi-two dimensional, there are three key directions, the direction of inhomogeneity (direction across the reconnection site), the direction of the reconnecting component of the magnetic field, and the direction of rough invariance (the "out of plane" direction). Using simulated spacecraft observations of an MHD simulation of magnetic reconnection in the geomagnetic tail, we test a direction-finding method based on the gradient of the vector magnetic field and find that the directions can be well determined. The results from this method, however, can be in error if there are systematic calibration errors in the magnetic field measurements. We show that the effect of these errors can be eliminated if an average gradient is subtracted from a time series of gradient values before they are used for the analysis. We also test a method to determine the velocity of the reconnecting structure relative to the spacecraft using the time derivative and gradient of the magnetic field and show that this velocity can be well determined. Calibration errors can be eliminated in this case also if an average time derivative and gradient are subtracted from the time series of values before they are used for the analysis.

**Citation:** Denton, R. E., B. U. Ö. Sonnerup, J. Birn, W.-L. Teh, J. F. Drake, M. Swisdak, M. Hesse, and W. Baumjohann (2010), Test of methods to infer the magnetic reconnection geometry from spacecraft data, *J. Geophys. Res.*, *115*, A10242, doi:10.1029/2010JA015420.

## 1. Introduction

[2] While there has been considerable research on methods to determine the direction across a one dimensional discontinuity from spacecraft observations [*Sonnerup et al.*, 2006, and references therein], there has been less research on methods to determine the orientation of two-dimensional structures. If a structure is approximately two dimensional, there will be a direction in which the variation is significantly less than that of the other directions. We call this the "invariant" or "out of plane" direction, recognizing however that in a real three-dimensional system, this invariance is only approximate. *Sonnerup and Hasegawa* [2005] developed a method based on Faraday's law to determine the orientation and motion of a two-dimensional time invariant structure. They determined an invariant direction and moving frame velocity that would minimize the variance of the out of plane component of the electric field in the frame of reference moving with the structure. This method requires a time series of electric and magnetic field observations, but can be used with observations from a single spacecraft.

[3] *Shi et al.* [2005] developed a method to determine three directions corresponding to maximum, intermediate, and minimum values of the squared magnitude of the vector magnetic field gradient. They called this technique "Minimum Direction Derivative (or Difference)," or MDD, analysis. This method requires field observations from four spacecraft in order to determine the gradient. A major advantage of this method is that it can yield the directions at each point in time using simultaneous magnetic field observations. *Shen et al.* [2003, 2007a, 2007b] used a similar approach based on the gradient of the magnetic field direction $\boldsymbol{b} \equiv \boldsymbol{B}/B$ that yields the maximum, intermediate, and minimum values of the squared curvature. Thus this technique tracks the field topology, rather than the gradient and curvature properties of the entire magnetic field. [We find better results (better separation in eigenvalues and steadier

[1]Department of Physics and Astronomy, Dartmouth College, Hanover, New Hampshire, USA.
[2]Thayer School of Engineering, Dartmouth College, Hanover, New Hampshire, USA.
[3]Los Alamos National Lab, Los Alamos, New Mexico, USA.
[4]Laboratory for Atmospheric and Space Physics, University of Colorado at Boulder, Boulder, Colorado, USA.
[5]Institute for Research and Electronics and Applied Physics, University of Maryland, College Park, Maryland, USA.
[6]NASA Goddard Space Flight Center, Greenbelt, Maryland, USA.
[7]Space Research Institute, Austrian Academy of Sciences, Graz, Austria.

Copyright 2010 by the American Geophysical Union.
0148-0227/10/2010JA015420

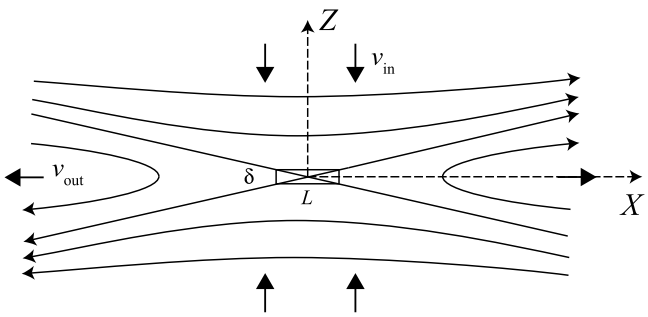


**Figure 1.** Sketch of reconnection geometry in the magnetotail. The $X$ point is at the origin of the $X$–$Z$ (SM) coordinate system. At large $|Z|$, the reconnecting magnetic field is oriented in the $X$ direction. Magnetic flux flows into the $X$ point from above and below with speed $v_{in}$ and out from the $X$ point to the right and left with speed $v_{out}$. The width of the diffusion region (rectangular box), $\delta$, is less than its length $L$, corresponding to greater gradient in the $Z$ direction.

eigenvectors) using the Shi et al. method, which is not surprising considering that the Shen et al. method does not make use of the additional information related to the magnetic field amplitude.] Assuming time stationarity ($d/dt = 0$) in the frame of the structure, *Shi et al.* [2006] used

$$\frac{d\boldsymbol{B}}{dt} = 0 = \frac{\partial \boldsymbol{B}}{\partial t} + (-\boldsymbol{V}_{\text{str}}) \cdot \nabla \boldsymbol{B} \rightarrow \frac{\partial \boldsymbol{B}}{\partial t} = \boldsymbol{V}_{\text{str}} \cdot \nabla \boldsymbol{B}, \tag{1}$$

where $d/dt$ ($\partial/\partial t$) is in the frame of the structure (spacecraft), and $-\boldsymbol{V}_{\text{str}}$ is the velocity of the structure frame relative to the spacecraft frame to determine the velocity $\boldsymbol{V}_{\text{str}}$ of a structure relative to the spacecraft. They called this technique "Spatiotemporal Difference" analysis, which they abbreviated as STD.

[4] In this paper, we will consider quasi-two dimensional reconnection, as illustrated in Figure 1. By "quasi-two dimensional," we mean that the system as a whole may be three dimensional, but the reconnection structure within it is approximately two dimensional; that is, the equilibrium (large-scale) gradients within the plane shown in Figure 1 are much larger than the gradients out of the plane. The direction of largest gradient in Figure 1 is across the current sheet, i.e., the $Z$ direction ($\hat{\boldsymbol{Z}}$) in Figure 1. The direction of intermediate gradient is along the reconnecting magnetic field, i.e., the $X$ direction ($\hat{\boldsymbol{X}}$) in Figure 1. The direction of minimum gradient is the third (out-of-plane) direction, i.e., the $Y$ direction ($\hat{\boldsymbol{Y}}$). We will use an MHD simulation of reconnection in the geomagnetic tail, performed by one of us (J.B.), in order to test the *Shi et al.* [2005, 2006] methods for determining the orientation and motion of the reconnection region. A set of four simulated spacecraft were flown through the simulations, and the fields observed by each spacecraft were recorded: the magnetic field $\boldsymbol{B}$; the electric field $\boldsymbol{E}$; the density $n$; the pressure $p$; and the fluid velocity $\boldsymbol{V}$. The vector fields were then rotated (by J.B.) into a Cartesian frame of reference ($x$, $y$, $z$) with arbitrarily chosen orientation and motion. The first author (R.D.) then analyzed the resulting data, with the objective of determining the orientation and motion of the reconnecting structure. MHD-based reconstruction of the configuration has also been performed and is reported separately (W.-L. Teh, et al., Resistive MHD reconstruction of two-dimensional coherent structures in space, submitted to Journal of Geophysical Research, 2010). We found early on that the *Sonnerup and Hasegawa* [2005] method cannot be used to determine the reconnection geometry for this simulation. The reason is that both the fluid velocity $\boldsymbol{V}$ and the magnetic field $\boldsymbol{B}$ lie approximately in the $X$-$Z$ plane so that $\boldsymbol{E} \sim -\boldsymbol{V} \times \boldsymbol{B}$ is dominantly in the $\hat{\boldsymbol{Y}}$ direction. (This is not precisely true because the simulation is only quasi-two-dimensional.) The Faraday's law method determines the $\hat{\boldsymbol{Y}}$ direction and event motion by finding that direction and velocity for which the variance of the component of the electric field in that direction is minimized. For our simulation, the electric field components in the $X$-$Z$ plane and their variances are very small. As a consequence, the method selects a direction other than $\hat{\boldsymbol{Y}}$ (for which the magnitude of that component of the electric field is small to begin with) as the minimum variance direction. Because of this, we use the *Shi et al.* [2005, 2006] method for all quantitative evaluation of the directions and motion. The possibility remains that the Faraday's law method might work in the presence of a guide field, $B_Y$, or for a non-MHD simulation for which there may be significant components of the electric field in the $X$-$Z$ plane.

[5] The initial analysis of the directions and event motion was done solely by use of the data provided, i.e., without knowledge of the true event orientation and motion in the simulations. That is, the study was a blind test. The test determined the directions of maximum, intermediate, and minimum gradient, $\hat{\boldsymbol{e}}_{\max}$, $\hat{\boldsymbol{e}}_{\text{int}}$, and $\hat{\boldsymbol{e}}_{\min}$, respectively, as well as the event velocity in the ($x$, $y$, $z$) frame, and then these were compared to the directions $\hat{\boldsymbol{Z}}$, $\hat{\boldsymbol{X}}$, and $\hat{\boldsymbol{Y}}$ and motion from the simulations, finding excellent agreement. Later, we examined the effect of random noise and calibration errors. It turned out that calibration errors could be a significant problem. Because of this, we developed a variation of the technique using the gradient of the magnetic field in which the average gradient is subtracted before the analysis. This further development was done after the real directions were known. In other words, this part of the analysis was not a blind test.

[6] In brief, we find that the method of *Shi et al.* [2005, 2006] is successful in determining the event orientation and velocity. Though calibration errors can cause this method to fail (particularly for finding the intermediate and minimum gradient directions), the method can work very well if an average gradient is subtracted before the analysis, as we will show. In section 2, we describe the noise and calibration errors; in section 3 we describe the method; in section 4 we describe the MHD simulation; in section 5, we present our results; and in section 6, we discuss the results.

## 2. Errors

[7] As described by *Georgescu et al.* [2006], Cluster spacecraft magnetic field data is stored with a precision of 0.008 nT for low $\boldsymbol{B}$ values ($\leq$64 nT), but that does not mean that the magnetic field measurements are that accurate. (Magnetic field data for the planned Magnetospheric Multiscale Mission [MMS] will be stored with a precision of

0.001 nT; estimates of noise and calibration errors should be similar to those for Cluster.) Random noise with standard deviation 0.01 nT is expected for each component of $\boldsymbol{B}$. As we will show, this noise is not a significant problem. The calibration error, however, is larger, typically about 0.1 nT for each component of $\boldsymbol{B}$. Not only is this value larger, but the greatest problem is that this is a systematic error. *Georgescu et al.* [2006] show that it is possible to reduce the errors for components in the spin frame with special calibration by the Electron Drift Instrument (EDI), perhaps to a value as low as 0.02 nT. In that case, the problem of the calibration error will be less serious. In the plasma sheet, this is difficult because the magnetic field is so small that EDI cannot be used. One can, however, calibrate using fields measured in previous and later time segments for which $B$ is larger, and this should make it possible to reduce the errors somewhat. There is another possibility for improving the calibration with MMS, for which the spacecraft separation will be much less than for Cluster (at least initially). In the lobe, the measurements from the different spacecraft should be almost identical, and the relative (between spacecraft) calibration errors (of most interest for this study) might be reduced significantly below 0.1 nT, perhaps as low as the noise error of 0.01 nT (Roy Torbert, private communication, 2010). At any rate, here we concentrate on the case of 0.1 nT calibration error for each component of $\boldsymbol{B}$. In the Discussion section, we'll make brief comments on the case of lower errors.

[8] There may also be errors associated with the calculation of the gradients. Basically, the spacecraft configuration needs to be roughly tetrahedral and the scale length for spatial variation needs to be significantly larger than the spacecraft separation in order for the gradients to be calculated accurately. We will not examine the effect of these issues.

## 3. Methods

### 3.1. Gradient Techniques

[9] If there are four spacecraft, as is the case for the Cluster and planned MMS missions, it is straightforward to calculate the gradient of scalar quantities such as density or pressure using the relative spacecraft positions. We have found this technique useful for giving a rough idea of the gradient directions but not very good for a quantitative measure.

[10] More information can be found by using the gradient of a vector quantity. *Shi et al.* [2005] describe the method using the gradient of the vector magnetic field. First the gradient of this field is calculated, and expressed as matrix $\mathbf{M}^{\nabla B}$, where $\mathbf{M}^{\nabla B}_{ik} = \partial_i B_k$, and $\partial_i$ is the spatial partial derivative in the $i$th direction. Then the symmetric matrix $\mathbf{M}^{\mathrm{G}} \equiv \mathbf{M}^{\nabla B} \cdot (\mathbf{M}^{\nabla B})^{\mathrm{T}}$ is formed, where "T" indicates the transpose of the matrix. The three eigenvalues, $\lambda_{\text{G-max}}$, $\lambda_{\text{G-int}}$, and $\lambda_{\text{G-min}}$, represent the maximum, intermediate, and minimum values of the squared directional derivative (gradient), with the eigenvectors $\hat{\boldsymbol{e}}_{\text{G-max}}$, $\hat{\boldsymbol{e}}_{\text{G-int}}$, and $\hat{\boldsymbol{e}}_{\text{G-min}}$ indicating the corresponding directions. These directions can be obtained at each time (without averaging) for which the $\boldsymbol{B}$ values are available. As *Shi et al.* [2005] explain, in order for the structure to be roughly two-dimensional, $\lambda_{\text{G-min}}$ should be significantly less than the other two eigenvalues. If $\lambda_{\text{G-max}} \gg \lambda_{\text{G-int}}, \lambda_{\text{G-min}}$, the structure is quasi-one-dimensional. If all the eigenvalues are comparable, the structure is fully three-dimensional, and the eigenvector directions may not be meaningful.

### 3.2. Technique Using the Perturbed Gradient $\delta\nabla\boldsymbol{B}$

[11] Note that as described, the *Shi et al.* [2005] technique yields the actual point by point gradients of $\boldsymbol{B}$. But relative inter-spacecraft calibration errors (differences in $\boldsymbol{B}$ measured by different spacecraft due to different calibration), being systematic, will lead to a systematic error in those gradients. If there are significantly large relative calibration errors, though we may be able to achieve at least a rough measure of the maximum gradient direction using the unmodified Shi et al. technique, the intermediate and minimum gradient directions inferred from the technique are likely to be significantly in error due to the spurious gradient of the calibration errors.

[12] We have found a way to eliminate the effect of calibration errors altogether. We will subtract off an average value of $\mathbf{M}^{\nabla B}$ ($=\nabla\boldsymbol{B}$) to get the perturbed magnetic field gradient $\delta\mathbf{M}^{\nabla B} \equiv \mathbf{M}^{\nabla B} - \langle \mathbf{M}^{\nabla B}\rangle_0$ ($=\delta\nabla\boldsymbol{B}$). We then use this perturbed value for the analysis in the same way as *Shi et al.* [2005]. We will normally measure this average value within an interval centered on the time at which $\mathbf{M}^{\nabla B}$ has its largest value (time of largest eigenvalue of $\mathbf{M}^{\mathrm{G}}$, since the largest eigenvalue of $\mathbf{M}^{\mathrm{G}}$ is the square of the amplitude of the largest value of $\nabla\boldsymbol{B}$). We will show results using different time intervals around the time of this maximum in order to show that the final results are not too sensitively dependent on the exact interval. Subtracting off the average value of $\mathbf{M}^{\nabla B}$ eliminates the effect of the calibration errors, since these errors lead to a constant gradient. We then average the time-dependent matrix $\delta\mathbf{M}^{\mathrm{G}} \equiv \delta\mathbf{M}^{\nabla B} \cdot (\delta\mathbf{M}^{\nabla B})^{\mathrm{T}}$, where we use $\langle\ \rangle$ to indicate an average, and where the "0" subscript indicates that this is the average used in the definition of the perturbed gradient, $\delta\mathbf{M}^{\nabla B} \equiv \mathbf{M}^{\nabla B} - \langle \mathbf{M}^{\nabla B}\rangle_0$. The averaging interval for $\langle\delta\mathbf{M}^{\mathrm{G}}\rangle$ may be (and usually will be) different than the averaging interval used for $\langle \mathbf{M}^{\nabla B}\rangle_0$. It seems to be best to average $\langle \mathbf{M}^{\nabla B}\rangle_0$ near the center of the current sheet where the gradient is large, whereas the minimum gradient direction is sometimes best found away from the current sheet. (See further discussion of this issue in section 7.) Having averaged $\langle\delta\mathbf{M}^{\mathrm{G}}\rangle$, we can then use the eigenvectors of $\langle\delta\mathbf{M}^{\mathrm{G}}\rangle$ to get the gradient directions.

[13] Even if the interval for averaging $\langle\delta\mathbf{M}^{\mathrm{G}}\rangle$ were the same as the one used for averaging $\langle \mathbf{M}^{\nabla B}\rangle_0$, we could still get information from $\langle\delta\mathbf{M}^{\mathrm{G}}\rangle$ because $\delta\mathbf{M}^{\mathrm{G}}$ is a nonlinear function of $\delta\mathbf{M}^{\nabla B}$. In that case,

$$\langle\delta \mathrm{M}^{\mathrm{G}}_{ij}\rangle = \left\langle \sum_k \delta \mathrm{M}^{\nabla B}_{ik} \left(\delta \mathrm{M}^{\nabla B}\right)^{\mathrm{T}}_{kj} \right\rangle \tag{2}$$

$$= \sum_k \langle \delta \mathrm{M}^{\nabla B}_{ik} \delta \mathrm{M}^{\nabla B}_{jk}\rangle \tag{3}$$

$$= \sum_k \left\langle \left(\mathrm{M}^{\nabla B}_{ik} - \langle \mathrm{M}^{\nabla B}_{ik}\rangle\right)\left(\mathrm{M}^{\nabla B}_{jk} - \langle \mathrm{M}^{\nabla B}_{jk}\rangle\right)\right\rangle \tag{4}$$

$$= \sum_k \left(\langle \mathrm{M}^{\nabla B}_{ik} \mathrm{M}^{\nabla B}_{jk}\rangle - \langle \mathrm{M}^{\nabla B}_{ik}\rangle\langle \mathrm{M}^{\nabla B}_{jk}\rangle\right), \tag{5}$$

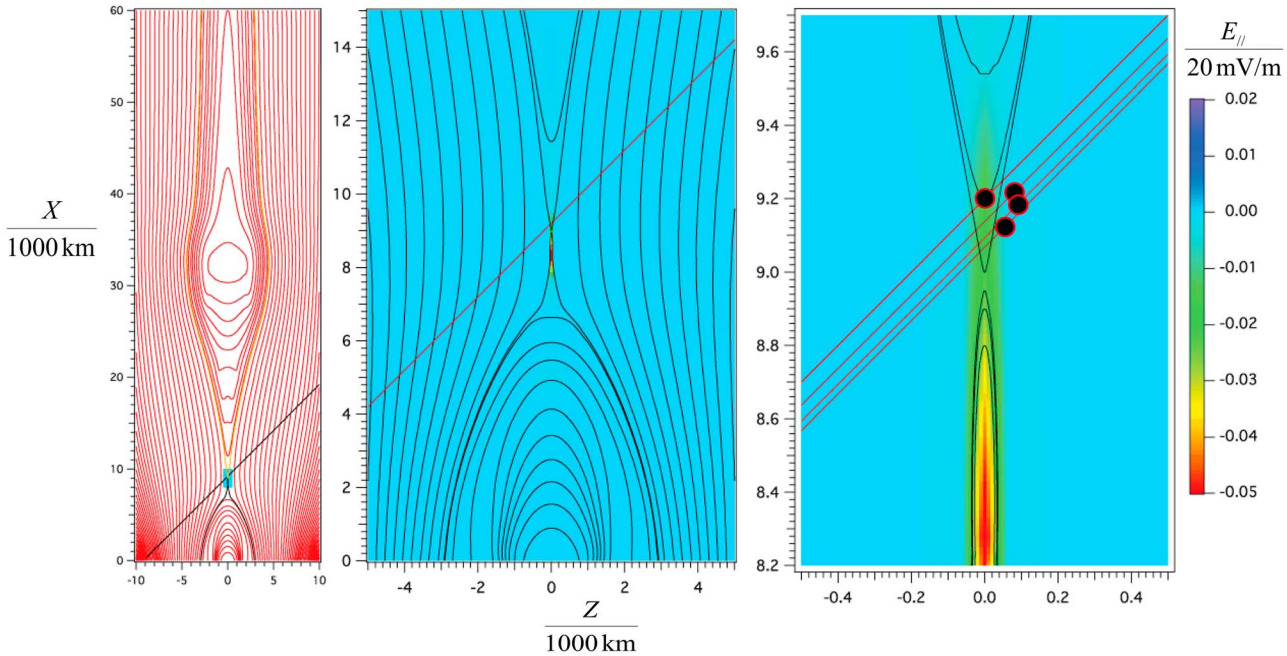


**Figure 2.** Snapshot of the MHD simulation used for this study. The red diagonal lines are the simulated spacecraft trajectories. (left) The entire simulation, (middle) a blowup of the region around the $X$ point, and (right) a further expansion in which the spacecraft separation can be resolved (instantaneous position indicated by the red circles filled with black). The simulation uses anomalous resistivity in the region where the component of the electric field parallel to the magnetic field $E_{\|}$ (color scale shown at right) is large.

showing that $\langle \delta \mathbf{M}^{\mathrm{G}} \rangle$ has the form of a mean squared deviation of $\mathbf{M}^{\nabla B}$. Therefore it is a measure of the variance in $\nabla \boldsymbol{B}$.

[14] We can also modify (1) in order to eliminate the effect of calibration errors. Using the average of $\nabla \boldsymbol{B}$ and the average of $\partial \boldsymbol{B}/\partial t$ (in the spacecraft frame) over the same time interval (note carefully that the time interval must be the same as for $\nabla \boldsymbol{B}$), $\boldsymbol{V}_{\mathrm{str}}$ can be found from

$$\delta\left(\frac{\partial \boldsymbol{B}}{\partial t}\right) = \boldsymbol{V}_{\mathrm{str}} \cdot \delta(\nabla \boldsymbol{B}), \tag{6}$$

where $\delta\ (\partial \boldsymbol{B}/\partial t) \equiv \partial \boldsymbol{B}/\partial t - \langle \partial \boldsymbol{B}/\partial t \rangle_0$, and $\delta\ (\nabla \boldsymbol{B}) \equiv \nabla \boldsymbol{B} - \langle \nabla \boldsymbol{B} \rangle_0$.

[15] So, the unmodified *Shi et al.* [2005, 2006] method uses the gradient of the entire magnetic field, $\nabla \boldsymbol{B}$, and the modified Shi et al. method uses the perturbed gradient of the magnetic field, $\delta \nabla \boldsymbol{B}$.

## 4. MHD Simulation

[16] Figure 2 shows a snapshot of the MHD simulation used for this study [*Birn and Hesse*, 2009]. For this first attempt to determine the reconnection geometry from simulated spacecraft data, virtual (simulated) spacecraft were flown across this snapshot with the trajectories shown in the figure so that the only time dependence of the recorded data was due to the motion of the spacecraft. (We discuss possible effects of explicit time dependence in section 7.) Anomalous resistivity was used in the region of the X point. The reconnection magnetic field ($X$ component) was 20 nT and the proton density was of order 0.08 cm$^{-3}$ in the current sheet, and 0.05 cm$^{-3}$ in the upstream region. This simulation had approximately zero guide field ($Y$ component of $\boldsymbol{B}$ in the midnight meridian plane). Figure 3 shows the fields measured by the virtual spacecraft.

## 5. Results

### 5.1. Scalar Gradients

[17] If our fluid simulation were exactly two dimensional (2D) and there were no errors, we could determine the minimum gradient direction as that direction for which the component of every gradient, including those of scalar quantities, is always zero. Because this simulation is 3D (only quasi-2D), this is not true. Furthermore, the varying spatial structure of scalar quantities can also complicate the apparent gradient directions. Because of these issues, we have not found gradients of scalar quantities to be useful for quantitatively determining the gradient directions. Nevertheless, they can at least be helpful for giving a general idea of these directions. Figure 4 shows the directions of the gradient of all available scalar fields, $n$, $p$, $Vx$, $Vy$, $Vz$, $Bx$, $By$, $Bz$, $Ex$, $Ey$, and $Ez$, measured during $t = -15$ to 25 s (near the current sheet crossing). To be included in the plot, each data point needed to be at least 1/10 as large as the largest gradient measured for each quantity. The gradient directions (dots) are plotted using a sinusoidal projection (sometimes used for maps of the Earth) for which the plotted area is proportional to the solid angle. The vertical axis of

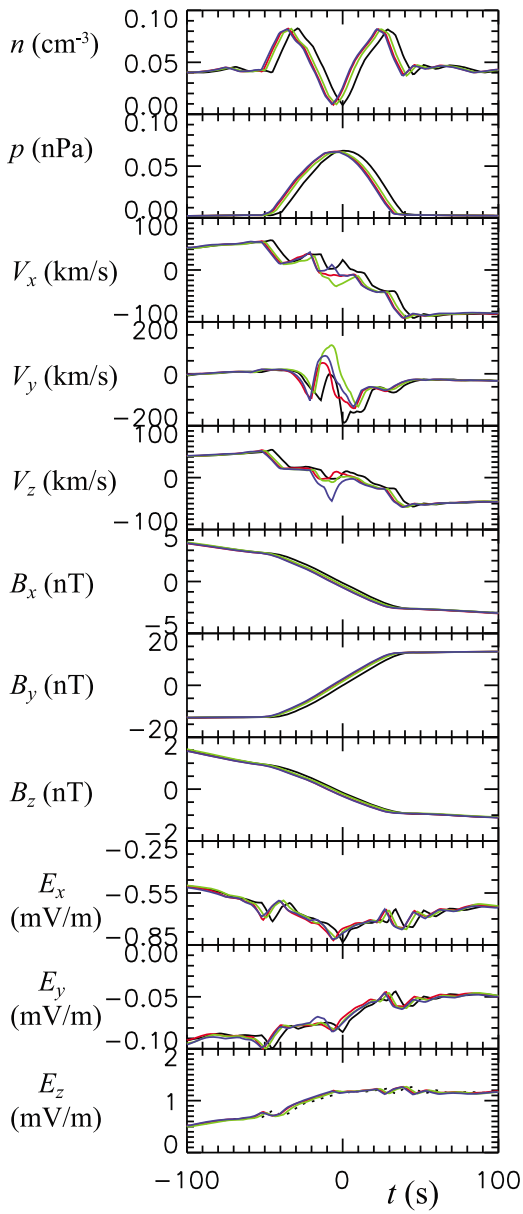


**Figure 3.** Virtual spacecraft measurements of density $n$, pressure $p$, and $x$, $y$, and $z$ components (arbitrary frame of reference) of the plasma velocity $\boldsymbol{V}$, the magnetic field $\boldsymbol{B}$, and the electric field $\boldsymbol{E}$ from the MHD simulation versus time $t$. The black, red, light green, and blue curves are for the individual spacecraft 1, 2, 3, and 4, respectively.

the plot is simply the polar angle $\theta$, but the horizontal axis is $90 + (\phi - 90)\sin\theta$, expressed in degrees. The upward pointing triangle, downward pointing triangle, and circle symbols in Figure 4 correspond to the exact $\hat{\boldsymbol{Z}}$, $\hat{\boldsymbol{X}}$, and $\hat{\boldsymbol{Y}}$ directions (presumed maximum, intermediate, and minimum gradient directions), respectively. Note that the upward pointing triangle (corresponding to the maximum gradient direction) is near the densest cluster of gradient directions, and the circle symbol (corresponding to the minimum gradient direction) is in the area that is most free of gradient measurements.

### 5.2. Directions From $\nabla\boldsymbol{B}$ Without Added Errors

[18] Figure 5a shows the eigenvalues from the *Shi et al.* [2005] technique using $\nabla\boldsymbol{B}$ for the entire time series of data, while Figures 5b–5d shows direction cosines for the eigenvector directions. (For instance, the black curve in Figure 5b shows the cosine of the angle between $\hat{\boldsymbol{e}}_{\text{G-max}}$ and $\hat{\boldsymbol{x}}$.) Reliable eigenvector directions can be found only if there is a significant separation between the eigenvalues. For instance, between $t = -300$ s and $-100$ s, the minimum gradient eigenvalue $\lambda_{\text{G-min}}$ (green curve in Figure 5a) is well separated from the other eigenvalues, and the direction cosines for $\hat{\boldsymbol{e}}_{\text{G-min}}$ (three curves in Figure 5d) have fairly steady values. On the other hand, the eigenvalues for the maximum and intermediate gradient, $\lambda_{\text{G-max}}$ and $\lambda_{\text{G-int}}$, respectively, are nearly the same; and during that time there are large oscillations in the directions of $\hat{\boldsymbol{e}}_{\text{G-max}}$ and $\hat{\boldsymbol{e}}_{\text{G-int}}$. Note that at the period of the current sheet crossing from about $t = -50$ to $+50$ s, the gradient in the magnetic field is large, indicated by a large peak in the maximum gradient eigenvalue. This period corresponds to the time that the virtual spacecraft are in the magnetic island (Figure 2, right).

[19] Now we zero in on the time period from $t = -15$ to 25 s (within the current sheet crossing), for which there is a fairly good separation in all three eigenvalues, and for which all the eigenvector directions are fairly steady. Figure 6 shows the eigenvalues and eigenvector directions as a function of time $t$ (curves) for this smaller segment of time. (The deep minimum in the minimum gradient eigenvalue (green curve) indicates that that value is approaching zero. This happens where the intermediate and minimum gradient components reverse direction. In other words, the gradient near this position has a single direction. The directions do not appear to change dramatically in Figure 6 because the vectors have been rotated to maintain continuity in sign.) In order to get directions characteristic of the entire time interval, we also

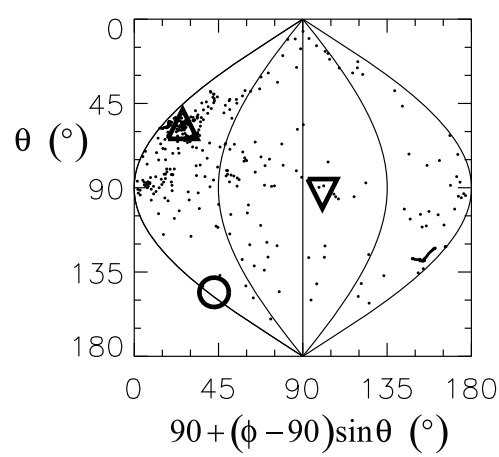


**Figure 4.** Sinusoidal projection of the polar ($\theta$, angle from $\hat{\boldsymbol{z}}$) and azimuthal ($\phi$, angle in the $x$–$y$ plane from $\hat{\boldsymbol{x}}$ toward $\hat{\boldsymbol{y}}$) angles in spherical coordinates. The curves extending from $\theta = 0°$ to 180° correspond from left to right to $\phi = 0°$, 45°, 90°, 135°, and 180°. The upward pointing triangle, downward pointing triangle, and circle symbols correspond to the exact $\hat{\boldsymbol{Z}}$, $\hat{\boldsymbol{X}}$, and $\hat{\boldsymbol{Y}}$ directions (presumed maximum, intermediate, and minimum gradient directions), respectively.

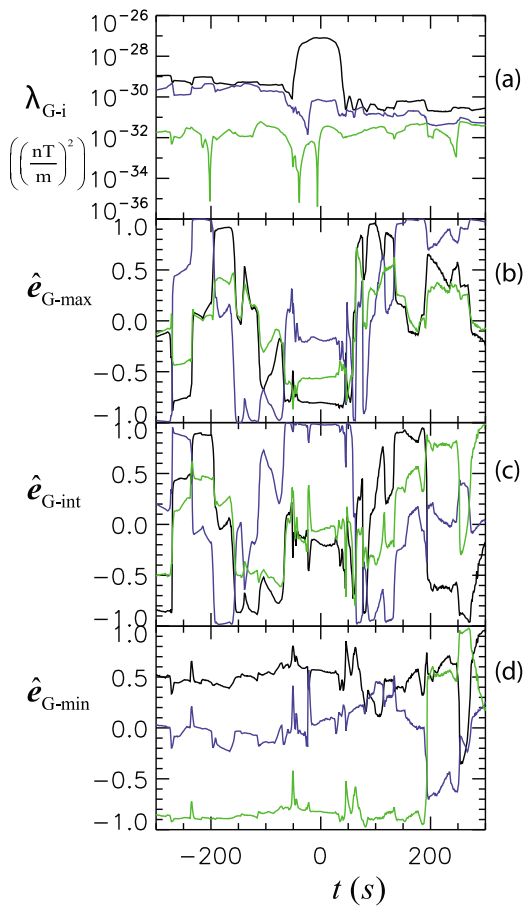


**Figure 5.** (a) Eigenvalues from the $\nabla \boldsymbol{B}$ [*Shi et al.*, 2005] method with black, blue, and green color corresponding to maximum, intermediate, and minimum gradient, respectively, (b) maximum gradient direction $\hat{\boldsymbol{e}}_{\text{G-max}}$, (c) intermediate gradient direction $\hat{\boldsymbol{e}}_{\text{G-int}}$, and (d) minimum gradient direction $\hat{\boldsymbol{e}}_{\text{G-min}}$, all versus time for the MHD simulation. The gradient directions are specified by the direction cosines with respect to the $x$ (black), $y$ (blue), and $z$ (green) directions.

found the eigenvectors of the time average of the matrix. The circle symbols in Figures 6b–6d are plotted at the midpoint of the time interval and vertically at the values of the direction cosines for these directions, showing that the eigenvectors using $\langle \mathbf{M}^{\text{G}} \rangle$ have a direction characteristic of the time series of the eigenvectors. After we did the analysis of these directions, we found the angular difference between the inferred directions $\hat{\boldsymbol{e}}_{\text{G-max}}$, $\hat{\boldsymbol{e}}_{\text{G-int}}$, and $\hat{\boldsymbol{e}}_{\text{G-min}}$, and the corresponding directions from the simulation, $\hat{\boldsymbol{Z}}$, $\hat{\boldsymbol{X}}$, and $\hat{\boldsymbol{Y}}$. These are listed as Case 1 (first row) in Table 1. Also listed in Table 1 (though not relevant to Case 1) are the standard deviation of the random (time varying) noise added to each component of the magnetic field, $dB_{i\text{-Noise}}$, the number of points on each side of a data point used for a boxcar average of the data $N_{\text{smoo}}$, the systematic calibration error (time invariant) added to each component of the magnetic field, $dB_{i\text{-Cal}}$, and the time interval used for calculating $\langle \mathbf{M}^{\nabla B} \rangle_0$ subtracted from $\mathbf{M}^{\nabla B}$ before forming $\delta \mathbf{M}^{\text{G}}$ (relevant when we use $\delta \nabla \boldsymbol{B}$ instead of $\nabla \boldsymbol{B}$). One should keep in mind here that the simulation is actually three-dimensional, so that $\hat{\boldsymbol{e}}_{\text{G-max}}$, $\hat{\boldsymbol{e}}_{\text{G-int}}$, and $\hat{\boldsymbol{e}}_{\text{G-min}}$ may not exactly correspond to $\hat{\boldsymbol{Z}}$, $\hat{\boldsymbol{X}}$, and $\hat{\boldsymbol{Y}}$. Nevertheless, as can be seen from Case 1 in Table 1, all the gradient directions agree to within 1° with the directions from the simulation.

[20] In this case, slightly more accurate directions can be found by taking the median of each component and then normalizing each direction to have unit magnitude. Since the maximum gradient direction is usually the most accurate, we subtract off that part of $\hat{\boldsymbol{e}}_{\text{G-min}}$ parallel to $\hat{\boldsymbol{e}}_{\text{G-max}}$, renormalize $\hat{\boldsymbol{e}}_{\text{G-min}}$, and then form $\hat{\boldsymbol{e}}_{\text{G-int}}$ from $\hat{\boldsymbol{e}}_{\text{G-min}} \times \hat{\boldsymbol{e}}_{\text{G-max}}$. The results are shown in Table 1 as Case 2. Here the gradient directions agree to within 0.75° with the corresponding directions from the simulation. Only for Case 2 are the directions calculated in this way. For other cases, we calculate the directions from the matrix $\langle \mathbf{M}^{\text{G}} \rangle$.

[21] While all three eigenvalue directions were fairly steady for $t = -15$ to 25s (Figure 6), the maximum eigenvalue direction is steady for a larger interval of time, at least from −40 to 30 s. Case 3 shows that the "error" in the maximum eigenvalue direction inferred using this time interval is 0.26°, slightly worse than that for $t = -15$ to 25 s (0.10°), but the results are almost exact in both cases. (Since there is some variation in the "out-of-plane" direction, this

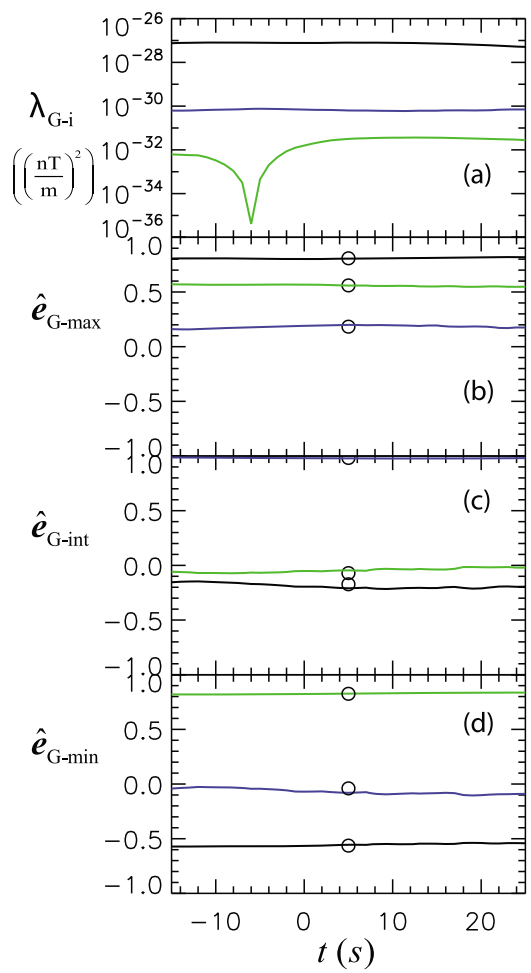


**Figure 6.** Same as Figure 5, but for $t = -15$ to 25 s. For each gradient direction, circle symbols are plotted at the midpoint of the time interval for the direction cosine with $\hat{\boldsymbol{x}}$, $\hat{\boldsymbol{y}}$, and $\hat{\boldsymbol{z}}$ using the matrix $\langle \mathbf{M}^{\text{G}} \rangle$.

**Table 1.** Angular Difference ∠ Between Directions Inferred by the $\nabla \boldsymbol{B}$ Method, $\hat{\boldsymbol{e}}_{\text{G-max}}$, $\hat{\boldsymbol{e}}_{\text{G-int}}$, and $\hat{\boldsymbol{e}}_{\text{G-min}}$, and the Corresponding Directions From the Simulation, $\hat{\boldsymbol{Z}}$, $\hat{\boldsymbol{X}}$, and $\hat{\boldsymbol{Y}}$, for the Cases Indicated

| Case | $t$[a] (s) | $dB_{i\text{-Noise}}$[b] (nT) | $N_{\text{smoo}}$[c] | $dB_{i\text{-Cal}}$[d] (nT) | $t_{\text{av}}$[e] (s) | $\angle(\hat{\boldsymbol{e}}_{\text{G-max}}, \hat{\boldsymbol{Z}})$[f] (°) | $\angle(\hat{\boldsymbol{e}}_{\text{G-int}}, \hat{\boldsymbol{X}})$[f] (°) | $\angle(\hat{\boldsymbol{e}}_{\text{G-min}}, \hat{\boldsymbol{Y}})$[f] (°) |
|---|---|---|---|---|---|---|---|---|
| 1 | [−15,25] | 0 | 0 | 0 | – | 0.10 | 1.0 | 1.0 |
| 2[g] | [−15,25] | 0 | 0 | 0 | – | 0.06 | 0.75 | 0.75 |
| 3 | [−40,30] | 0 | 0 | 0 | – | 0.26 | – | – |
| 4 | [−300, −100] | 0 | 0 | 0 | – | – | – | 8.3 |
| 5 | [−15,25] | 0.01 | 0 | 0 | – | 0.13 | 1.6 | 1.6 |
| 6 | [−15,25] | 0.01 | 10 | 0 | – | 0.11 | 1.8 | 1.8 |
| 7 | [−30,25] | 0 | 0 | 0.1 | – | 4.6 | 63. | 63. |
| 8 | [−170, −70] | 0 | 0 | 0.1 | – | – | – | 75. |
| 9 | [100,300] | 0 | 0 | 0.1 | – | – | – | 79. |
| 10 | [−30,25] | 0 | 0 | 0.1 | −9 ± 50 | 0.45 | – | – |
| 11 | [−30,25] | 0 | 0 | 0.1 | −9 ± 100 | 0.78 | – | – |
| 12 | [−30,25] | 0 | 0 | 0.1 | −9 ± 200 | 0.38 | – | – |
| 13 | [−30,25] | 0 | 0 | 0.1 | −9±300 | 0.85 | – | – |
| 14 | [−30,25] | 0 | 0 | 0.1 | −9 ± 400 | 1.2 | – | – |
| 15 | [−30,25] | 0 | 0 | 0.1 | −9 ± 500 | 1.5 | – | – |
| 16 | [350,700] | 0 | 0 | 0.1 | −9 ± 50 | 0.45 | 2.1 | 2.1 |
| 17 | [350,700] | 0 | 0 | 0.1 | −9 ± 100 | 0.31 | 3.7 | 3.7 |
| 18 | [350,700] | 0 | 0 | 0.1 | −9 ± 200 | 1.9 | 6.3 | 6.0 |
| 19 | [350,700] | 0 | 0 | 0.1 | −9 ± 300 | 5.7 | 8.0 | 5.6 |
| 20 | [350,700] | 0 | 0 | 0.1 | −9 ± 400 | 10. | 12. | 6.5 |
| 21 | [350,700] | 0 | 0 | 0.1 | −9 ± 500 | 15. | 16. | 7.2 |
| 22 | mixed[h] | 0 | 0 | 0.1 | −9 ± 500 | 1.5 | 7.1 | 6.9 |
| 23 | mixed[h] | 0.01 | 0 | 0.1 | −9 ± 500 | 1.5,1.5,1.5[i] | 6.9,7.2,7.7[i] | 6.8,7.0,7.5[i] |
| 24 | mixed[h] | 0.01 | 20 | 0.1 | −9 ± 500 | 1.5,1.5,1.5[i] | 5.8,6.3,7.0[i] | 5.7,6.0,6.9[i] |
| 25 | mixed[h] | 0.01 | 20 | 0.1 | −9 ± 50 | 0.31,0.37,0.39[i] | 0.77,1.4,1.9[i] | 0.76,1.4,1.9[i] |
| 26 | [350,700] | 0 | 0 | 0.1 | [350,700] | 14. | 14. | 7.3 |
| 27 | [590,630] | 0 | 0 | 0.1 | [350,700] | 3.2 | 22. | 23. |

[a]Inclusive limits of time range ($t$) used.
[b]Amplitude of random Gaussian noise (time varying) added to each component of $\boldsymbol{B}$ before analysis.
[c]Boxcar average of input data is done using each data point plus $N_{\text{smoo}}$ data points on either side.
[d]Amplitude of random Gaussian error (time-invariant calibration error) added to each component of $\boldsymbol{B}$ before analysis.
[e]If this entry is not "–," it indicates a time range over which $\nabla \boldsymbol{B}$ is averaged; this average is subtracted from the instantaneous value of $\nabla \boldsymbol{B}$ before the analysis.
[f]Angle between the argument vectors in degrees.
[g]Here only, the directions are found by taking the median of each instantaneous component.
[h]Using $t$ = (−30, 25) for evaluation of $\hat{\boldsymbol{e}}_{\text{G-max}}$ and $t$ = (350,700) for evaluation of $\hat{\boldsymbol{e}}_{\text{G-min}}$, subtracting off the part of $\hat{\boldsymbol{e}}_{\text{G-min}}$ parallel to $\hat{\boldsymbol{e}}_{\text{G-max}}$, and then taking $\hat{\boldsymbol{e}}_{\text{G-int}} = \hat{\boldsymbol{e}}_{\text{G-min}} \times \hat{\boldsymbol{e}}_{\text{G-max}}$.
[i]First quartile, median, and third quartile values for an ensemble of 21 trials using different random noise.

level of angular difference may or may not be a real error.) Case 4 shows the error in the minimum gradient direction calculated using the interval $t$ = −300 to −100 s during which the minimum eigenvalue is well separated from the intermediate eigenvalue (Figure 5a). The direction cosines for the minimum gradient direction are not totally steady during this time (Figure 5d), however, and the error in $\hat{\boldsymbol{e}}_{\text{G-min}}$ found using this time interval (8.3°) is larger than that using the shorter interval $t$ = −15 to 25 s (1°).

### 5.3. Directions From $\nabla \boldsymbol{B}$ With Errors

[22] As mentioned in section 2, the magnetic field measurements on Cluster and MMS are subject to two kinds of errors. The first kind is random (time varying) noise, and for low values of the magnetic field amplitude, this error is on the order of 0.01 nT for each component. In Cases 5 and 6 in Table 1, we add random errors with a standard deviation of 0.01 nT to each data point for each component. The difference between Case 5 and 6 is that for Case 6, we do a running boxcar average of the magnetic field measurements at each data point using $N_{\text{smoo}}$ = 10 data points on either side (average of 21 surrounding values at each central point). This results in more steady instantaneous values of the directions (not shown). The results are almost the same in either case, however, slightly worse than that for no noise (Case 1), but still very good with errors less than or equal to 1.8°. In general, we find that this level of random noise (0.01 nT) is not a serious problem.

[23] While random noise is not a serious problem when using $\nabla \boldsymbol{B}$, calibration errors at a level of 0.1 nT (section 2) are a problem, at least for the case of 20 nT antiparallel reconnecting field considered here. Figure 7 shows the same information as was plotted in Figure 5, but with calibration errors with a standard deviation of 0.1 nT added to each component of the magnetic field before the analysis. Note that the particular results in Figure 7 are dependent on the random values of the error. If our final method depended on the exact errors, we would examine a statistical ensemble of cases with different errors in order to evaluate the success of the method. We will find, however that it is possible to eliminate these errors, so we will not do such a study. The purpose of Figure 7 is to show that, with a particular choice of errors, the results using $\nabla \boldsymbol{B}$ are significantly contaminated.

[24] A quick comparison of Figure 7 to Figure 5 shows a significant difference. The gradient directions calculated with the calibration errors are steadier over longer periods of time. This is because of the constant gradient due to the errors; the constant gradients heavily influence the eigenvector directions calculated from $\nabla \boldsymbol{B}$ using $\langle \mathbf{M}^{\text{G}} \rangle$ as

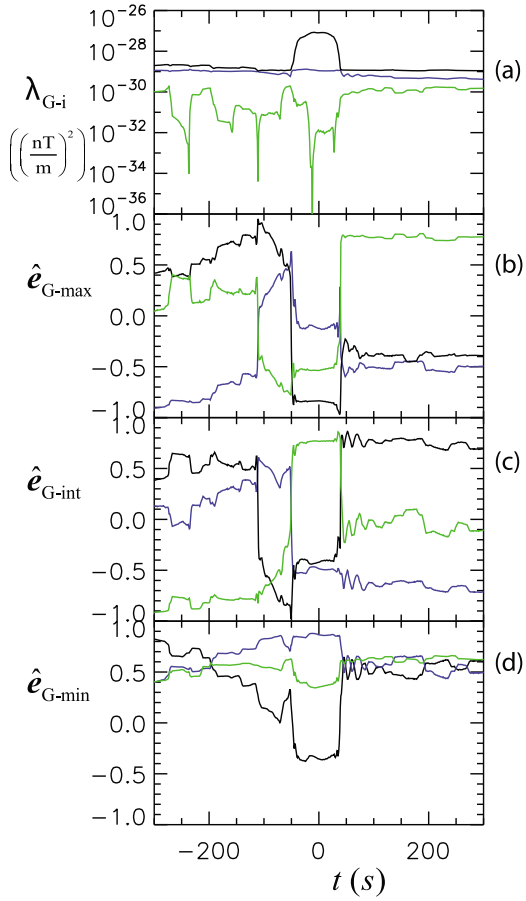


**Figure 7.** Same as Figure 5, but now systematic calibration errors (time invariant) have been added to each component of the magnetic field before the analysis.

discussed in section 2. For the data with calibration errors, all three eigenvector directions are steady over a somewhat larger period of time near $t = 0$, from −30 to 25 s, than was used for Case 1 (−15 to 25 s). Case 7 in Table 1 shows the errors in the angles. They are 4.6° for $\hat{\boldsymbol{e}}_{G\text{-max}}$, but 63° for $\hat{\boldsymbol{e}}_{G\text{-int}}$ and $\hat{\boldsymbol{e}}_{G\text{-min}}$. For Cases 8 and 9, we tried different intervals to find the minimum gradient direction $\hat{\boldsymbol{e}}_{G\text{-min}}$, but the errors are just as bad, 75° and 79°, respectively. Apparently calibration errors at a level of 0.1 nT are not large enough to completely destroy information about the maximum eigenvector direction (for which the associated gradient is largest), but these errors do contaminate the gradients in the intermediate and minimum eigenvector directions so that these directions are no longer useful as predictors of $\hat{\boldsymbol{X}}$ and $\hat{\boldsymbol{Y}}$.

### 5.4. Directions From $\delta\nabla\boldsymbol{B}$

[25] As mentioned in section 3.2, it should be possible to reduce the calibration errors through special calibration using EDI (on Cluster or MMS). If, however, the errors are as large as 0.1 nT, using $\nabla\boldsymbol{B}$ will not be good enough. In order to deal with this problem, we modified the *Shi et al.* [2005] method by using $\delta\nabla\boldsymbol{B}$ (the perturbed gradient), as was discussed in section 3.2. This method subtracts off the average value of $\nabla\boldsymbol{B}$ within a time interval centered about the maximum gradient, and thereby totally eliminates any time-independent gradient, such as that created by the calibration errors. Roughly, this method calculates the gradient directions using the mean squared deviation of $\mathbf{M}^G$ (like in minimum variance analysis; see discussion in section 3.2).

[26] Figure 8 shows the gradient eigenvalues and directions for $\delta\mathbf{M}^G$ calculated from $\delta\mathbf{M}^{\nabla B} = \mathbf{M}^{\nabla B} - \langle\mathbf{M}^{\nabla B}\rangle_0$, with the $\langle\ \rangle_0$ averaging interval $t_{av} = -9 \pm 100$ s. As already mentioned, the curves shown in this plot are totally independent of any calibration errors, since average gradients have been subtracted off from $\nabla\boldsymbol{B}$ before the analysis.

[27] Cases 10 through 27 show results using $\delta\nabla\boldsymbol{B}$. The time interval used to determine the average value of $\nabla\boldsymbol{B}$ to be subtracted is shown in the column labeled $t_{av}$. As mentioned in section 3.2, we average $\nabla\boldsymbol{B}$ in a time interval centered on the time at which $\nabla\boldsymbol{B}$ has its largest value (time of the largest eigenvalue of $\mathbf{M}^G$). The peak value of the largest eigenvalue of $\mathbf{M}^G$ occurs at about $t = -9$ s, as can be seen from the black curve in Figure 5a.

[28] In Figure 8, the maximum gradient direction is fairly steady in a middle range of times, $t = -30$ to 25 s, and also at late times $t > 50$ s. (The direction is not greatly different between these two time periods; there is a reversal in the direction indicated by a change in sign of all the direction cosines. Such a change is not relevant.) First we look at the error in the maximum gradient direction $\hat{\boldsymbol{e}}_{G\text{-max}}$ within the central time interval $t = -30$ to 25 s. Cases 10 through 15 in Table 1 show the difference in the angle between $\hat{\boldsymbol{e}}_{G\text{-max}}$ and

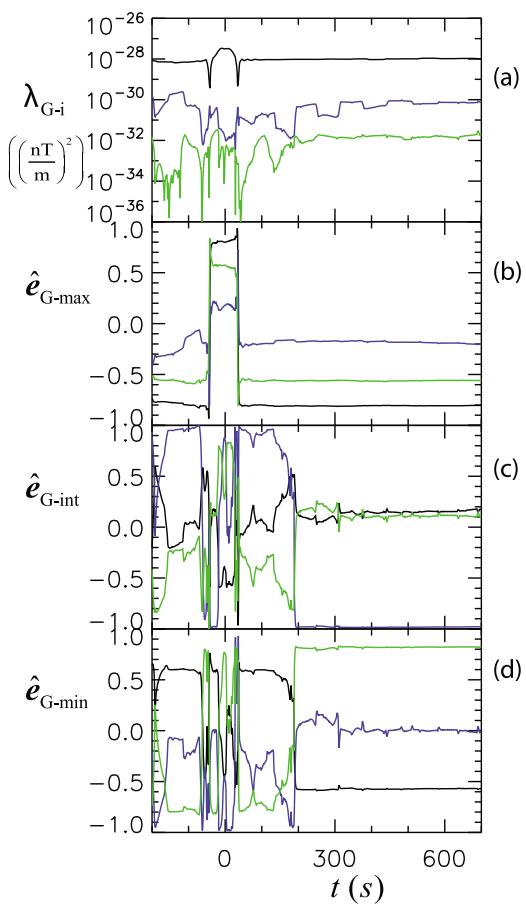


**Figure 8.** Same as Figure 5, but based on the perturbed gradient method using $\delta\mathbf{M}^G$ calculated from $\delta\mathbf{M}^{\nabla B} = \mathbf{M}^{\nabla B} - \langle\mathbf{M}^{\nabla B}\rangle_0$, with the $\langle\ \rangle_0$ averaging interval $t_{av} = -9 \pm 100$ s.

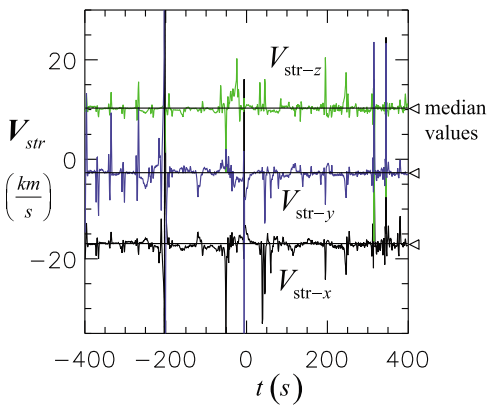


**Figure 9.** Values of $V_{str\text{-}x}$ (solid curve), $V_{str\text{-}y}$ (dashed curve), and $V_{str\text{-}z}$ (dotted curve) versus time $t$ solving for $\boldsymbol{V}_{str}$ from (1). The left pointing triangles at the right of the plot are vertically centered on the median values of each component; the horizontal lines are located vertically at the exact values of the components.

$\hat{\boldsymbol{Z}}$, $\angle$ ($\hat{\boldsymbol{e}}_{G\text{-max}}$, $\hat{\boldsymbol{Z}}$), using $\delta\nabla\boldsymbol{B}$ with different time intervals around the time of the largest gradient at $t = -9$ s to determine $\langle \mathbf{M}^{\nabla B}\rangle_0$. The error varies from 0.45° for the time interval −9 ± 50 s to 1.5° for the time interval −9 ± 500 s. So while there is some dependence on the exact time interval, the errors are small regardless which time interval is used.

[29] The maximum gradient direction can also be found at late times (Figure 8a). The three directions are particularly well defined at $t$ = 350 to 700s. Cases 16 through 21 show the errors in the three angles, $\hat{\boldsymbol{e}}_{G\text{-max}}$, $\hat{\boldsymbol{e}}_{G\text{-int}}$, and $\hat{\boldsymbol{e}}_{G\text{-min}}$, for different choices of the time interval used to calculate $\langle \mathbf{M}^{\nabla B}\rangle_0$. The errors are smallest for the averaging interval $t = -9 \pm 50$ s, 0.45°, 2.1°, and 2.1°, respectively, for $\hat{\boldsymbol{e}}_{G\text{-max}}$, $\hat{\boldsymbol{e}}_{G\text{-int}}$, and $\hat{\boldsymbol{e}}_{G\text{-min}}$, and the errors are largest for −9 ± 500 s, 15°, 16°, and 7.2°.

[30] Case 22 shows that even with a poor choice of the averaging interval to determine $\langle \mathbf{M}^{\nabla B}\rangle_0$ (−9 ± 500 s, for which the errors in the angles are largest), better results can be found by using the maximum gradient direction found at the time of its largest value ($t$ = −30 to 25 s) along with the minimum gradient direction found at the time away from the largest gradients ($t$ = 350 to 700s). In this case, we subtracted off the part of $\hat{\boldsymbol{e}}_{G\text{-min}}$ that was parallel to $\hat{\boldsymbol{e}}_{G\text{-max}}$ (considering $\hat{\boldsymbol{e}}_{G\text{-max}}$ to be best determined), and then after renormalizing $\hat{\boldsymbol{e}}_{G\text{-min}}$ found $\hat{\boldsymbol{e}}_{G\text{-int}} = \hat{\boldsymbol{e}}_{G\text{-min}} \times \hat{\boldsymbol{e}}_{G\text{-max}}$. In this case all errors were less than or equal to 7.1°. Cases 23 and 24 add random noise with $dB_{i\text{-Noise}}$ = 0.01 nT (same noise level as before). Here, in order to account for random differences, we examine an ensemble of 21 trials. The errors in the angles shown in the last three columns of Table 1 are the first quartile, median, and last quartile values (6th, 11th, and 16th values out of 21 when arranged in order from smallest to largest). The maximum gradient direction is very well defined with a largest error of 1.5°. The median values for the other angles are no larger than 7.2° (with a smaller error = 1.5° for the normal direction). Case 25 shows the results for a better choice of averaging interval (−9 ± 50 s), for which the median values of the errors are all no greater than 1.4°. These results suggest that a good choice for the averaging time interval is the time encompassing the peak in the largest eigenvalue, which is about −9 ± 50 as seen from the black curve in Figure 5a.

## 6. Structure Velocity

[31] As mentioned in section 1, we can solve for $\boldsymbol{V}_{str}$ at each data point using (1), namely $\partial\boldsymbol{B}/\partial t = \boldsymbol{V}_{str} \cdot \nabla\boldsymbol{B}$. Figure 9 shows the time series of the velocity components of $\boldsymbol{V}_{str}$ in the arbitrary $x$-$y$-$z$ frame versus time $t$ for the time interval

**Table 2.** Percentage Difference $\Delta(V_{str}, V_{str}^{\nabla B})$ Between the Magnitude of the Actual Structure Velocity $V_{str}$ and That Inferred Using $\nabla\boldsymbol{B}$, $V_{str}^{\nabla B}$, and the Angular Difference $\angle$ ($\hat{\boldsymbol{e}}_{Vstr}$, $\hat{\boldsymbol{e}}_{Vstr}^{\nabla B}$) Between $\hat{\boldsymbol{e}}_{Vstr}$ and $\hat{\boldsymbol{e}}_{Vstr}^{\nabla B}$ for the Cases Indicated

| Case | $t$[a] (s) | $dB_{i\text{-Noise}}$[b] (nT) | $N_{smoo}$[c] | $dB_{i\text{-Cal}}$[d] (nT) | $t_{av}$[e] (s) | $\Delta(V_{str}, V_{str}^{\nabla B})$[f] (%) | $\angle$ ($\hat{\boldsymbol{e}}_{Vstr}$, $\hat{\boldsymbol{e}}_{Vstr}^{\nabla B}$)[g] (°) |
|---|---|---|---|---|---|---|---|
| 26 | [−400,400] | 0 | 0 | 0 | – | 0.60 | 0.53 |
| 27 | [−400,400] | 0.01 | 0 | 0 | – | 7.9 | 8.5 |
| 28 | [−400,400] | 0.01 | 25 | 0 | – | 4.9 | 1.7 |
| 29 | [−400,400] | 0.01 | 50 | 0 | – | 1.5 | 0.14 |
| 30 | [−400,400] | 0.01 | 100 | 0 | – | 2.2 | 2.0 |
| 31 | [−400,400] | 0.01 | 200 | 0 | – | 0.91 | 1.0 |
| 32 | [−400,400] | 0.01 | 400 | 0 | – | 0.50 | 0.87 |
| 33 | [−400,400] | 0 | 0 | 0.1 | – | 68. | 46. |
| 34 | [−400,400] | 0 | 0 | 0.1 | −9 ± 50 | 0.03 | 0.18 |
| 35 | [−400,400] | 0 | 0 | 0.1 | −9 ± 100 | 0.02 | 0.14 |
| 36 | [−400,400] | 0 | 0 | 0.1 | −9 ± 200 | 0.03 | 0.21 |
| 37 | [−400,400] | 0 | 0 | 0.1 | −9 ± 300 | 0.18 | 0.12 |
| 38 | [−400,400] | 0 | 0 | 0.1 | −9 ± 400 | 0.04 | 0.35 |
| 39 | [−400,400] | 0.01 | 100 | 0.1 | −9 ± 50 | 0.75 | 1.8 |
| 40 | [−400,400] | 0.01 | 100 | 0.1 | −9 ± 50 | 0.75,1.6,3.0[h] | 1.8,2.1,3.5[h] |

[a]Inclusive limits of time range ($t$) used.
[b]Amplitude of random Gaussian noise (time varying) added to each component of $\boldsymbol{B}$ before analysis.
[c]Boxcar average of input data is done using each data point plus $N_{smoo}$ data points on either side.
[d]Amplitude of random Gaussian error (time invariant calibration error) added to each component of $\boldsymbol{B}$ before analysis.
[e]If this entry is not "–," it indicates a time range over which $\nabla\boldsymbol{B}$ is averaged; this average is subtracted from the instantaneous value of $\nabla\boldsymbol{B}$ before the analysis.
[f]Percentage difference from $\boldsymbol{V}_{str}$ to $\boldsymbol{V}_{str}^{\nabla B}$.
[g]Angle between $\hat{\boldsymbol{e}}_{Vstr}$ and $\hat{\boldsymbol{e}}_{Vstr}^{\nabla B}$ in degrees.
[h]First quartile, median, and third quartile values for an ensemble of 21 trials using different random noise.

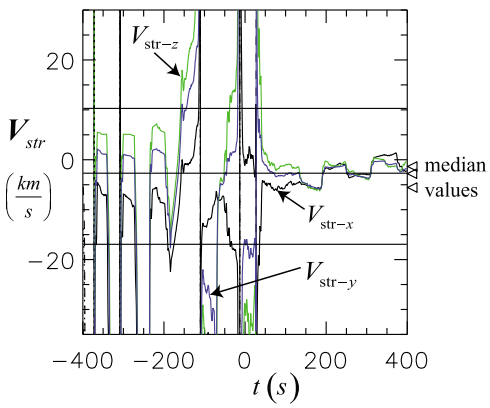


**Figure 10.** Same as Figure 9, but for Case 33 using the unmodified *Shi et al.* [2006] ($\nabla\boldsymbol{B}$) method with $dB_{i\text{-Cal}}$ = 0.1 nT.

−400 to 400 s. Most of these instantaneous values are very close to the exact values indicated by the horizontal lines. There are, however, a number of spikes in the components. These are caused by data points for which components of $\nabla\boldsymbol{B}$ become small, so that $\boldsymbol{V}_{\text{str}}$ is ill defined (see section 5.3). In order to get a typical value that we can compare to the known exact values, we take the median value of each component. (Using the median value rather than the mean reduces the effect of the outlier points within the spikes.) The left pointing triangles at Figure 9 (right) are plotted vertically at the position of these median values. It is clear that these values are in good agreement with the exact values indicated by the horizontal lines.

[32] To get a more quantitative measure of the agreement, we list in Table 2 the percent difference from the exact magnitude of the vector $\boldsymbol{V}_{\text{str}}$, $V_{\text{str}}$, to the magnitude of the vector $\boldsymbol{V}_{\text{str}}^{\nabla\boldsymbol{B}}$ (combination of median component values) determined using (1), $V_{\text{str}}^{\nabla\boldsymbol{B}}$, and the angle $\tilde{\mathrm{O}}(\hat{\boldsymbol{e}}_{\text{Vstr}}, \hat{\boldsymbol{e}}_{\text{Vstr}}^{\nabla\boldsymbol{B}})$ between the exact $\boldsymbol{V}_{\text{str}}$ and $\boldsymbol{V}_{\text{str}}^{\nabla\boldsymbol{B}}$. Case 26 shows the results with no added errors (noise or calibration errors). The difference in the magnitudes is 0.60% and the difference in the angles is 0.53°. Since the velocity is exactly known, these are a measure of error. These small numbers, however clearly indicate excellent agreement, as was also clear from Figure 9. Even better agreement can be found using the entire time interval for which the data was available. In general, we find a better value by using a larger time interval.

[33] Cases 27–32 show how the results are modified if random (time varying) noise is added to each component of the magnetic field with standard deviation $dB_{i\text{-Noise}}$ = 0.01 nT. In Case 27, the noise is added with no modification to the analysis. In that case the error in the inferred magnitude is 7.9% and error in the inferred angle is 8.5°. Cases 28–32 show that the errors decrease markedly if the data is smoothed using a boxcar average with the central data point and $N_{\text{smoo}}$ data points on either side. Using smoothing over a very large span ($N_{\text{smoo}} \geq 200$ for Cases 31 and 32), the error in magnitude is less than or equal to 1% and the error in the angle is less than or equal to 1°, which we consider to be quite good accuracy.

[34] Cases 33–40 show how the results are modified if systematic (time invariant) calibration errors are included with a standard deviation of $dB_{i\text{-Cal}}$ = 0.1 nT. For these Cases, we use the default random number sequence of Matlab to generate the calibration and noise errors. Case 33 shows the result using $\nabla\boldsymbol{B}$. The error in the magnitude of $V_{\text{str}}^{\nabla B}$ is now 68% and the error in the angle is 46°. These large errors result from the fact that $\nabla\boldsymbol{B}$ is systematically in error (see Figure 10), leading to bad values for the inferred $V_{\text{str}}^{\nabla B}$. The component of $V_{\text{str}}^{\nabla B}$ in the maximum gradient direction will not be greatly in error, but the components in the intermediate and minimum gradient directions are severely contaminated. These large errors can be immensely reduced by using $\delta\nabla\boldsymbol{B}$ as was described in section 3.2. Cases 34-38 show results for which the average values of $\nabla\boldsymbol{B}$ and $\partial\boldsymbol{B}/\partial t$ have been subtracted from $\nabla\boldsymbol{B}$ and $\partial\boldsymbol{B}/\partial t$ before the analysis using (6). The difference in these cases is the averaging time interval $t_{\text{av}}$. The results are excellent regardless of what averaging interval is used. All the errors in the magnitude of $V_{\text{str}}^{\nabla B}$ are less than or equal to 0.2%, and all the errors in the angle are less than or equal to 0.35°. Figure 11 shows the time-dependent velocity components for Case 35 with $t_{\text{av}} = -9 \pm 100$ s. The consistency of the inferred structure velocity is quite similar to that of Case 26 with no calibration errors (Figure 9).

[35] Cases 39 shows the effect of using both random noise and calibration errors. The error in the magnitude of $\boldsymbol{V}_{\text{str}}^{\nabla\boldsymbol{B}}$ is 0.75%, and the error in the angle in 1.8°. Finally, Case 40 shows the results of an ensemble of 21 trials using different calibration and noise errors. The three numbers listed for the error in the magnitude and angle are the first quartile, median and third quartile values. (See the explanation of Table 1 in section 5.3.) The median value for the error in magnitude is 1.6%, and the median value of the error in the angle is 2.1°, still quite acceptable.

## 7. Discussion

[36] Our results suggest that if the calibration errors can be ignored, the unmodified *Shi et al.* [2005] and *Shi et al.* [2006] methods using $\nabla\boldsymbol{B}$ can be used to calculate the directions and velocities quite accurately (Table 1, Case 1; Table 2, Case 26). The results for the directions do depend

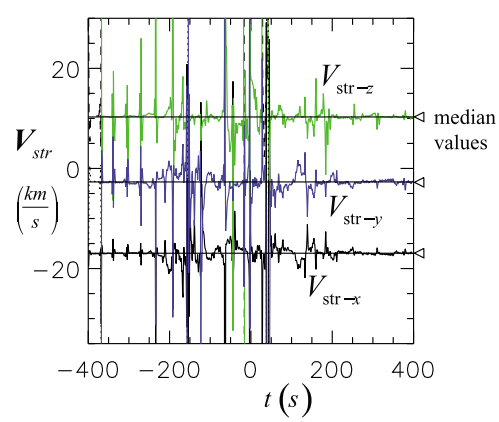


**Figure 11.** Same as Figure 9, but for Case 35 using the perturbed $\nabla\boldsymbol{B}$ method with $dB_{i\text{-Cal}}$ = 0.1 nT and with the averaging interval for $\nabla\boldsymbol{B}$ and $\partial\boldsymbol{B}/\partial t$ equal to $t_{\text{av}} = -9 \pm 100$ s.

on the time interval used for analysis ($t$ in Table 1). The best results seem to occur when there is a good separation of the eigenvalues of $\mathbf{M}^{\mathrm{G}}$ and when the eigenvector directions are relatively stable. For Case 4 in Table 1 using the time interval $t = -300$ to $-100$ s, there is a good separation for the minimum gradient eigenvalue (low value of $\lambda_{\text{G-min}}$ in Figure 5a, green curve), but the direction cosines for $\hat{\boldsymbol{e}}_{\text{G-min}}$ show a fairly large variation; and the error in the direction of $\hat{\boldsymbol{e}}_{\text{G-min}}$ for this case is significantly larger (8.3°) than that for case 1 (1.0°).

[37] Random noise errors in the magnetic field components do not significantly affect the inferred directions (Table 1, Cases 5 and 6). They do, however significantly affect the accuracy of the inferred structure velocity (Table 1, Case 27). This problem can be easily dealt with by smoothing the data (Table 2, Cases 28–32). Calibration errors, which are systematic (time invariant), present a more serious problem. If the reconnecting magnetic field is larger than we have assumed (20 nT upstream of the diffusion region), or if the calibration errors can be reduced (see section 2), the results using $\nabla \boldsymbol{B}$ will be improved, but we find errors of 5 to 10° (depending on the interval analyzed) for the intermediate and minimum gradient directions using the unmodified method even with calibration errors as low as 0.01 nT.

[38] To negate the effect of the calibration errors, we modified the *Shi et al.* [2005] and *Shi et al.* [2006] methods to use $\delta\nabla \boldsymbol{B}$ (the perturbed gradient; see section 3.2). Basically, the average gradient over some time period is subtracted from the instantaneous gradient, and the resulting perturbed gradient is used in the analysis. As shown in section 3.2, this method uses a quantity roughly equal to the mean squared deviation of the matrix $\mathbf{M}^{\mathrm{G}} \equiv \mathbf{M}^{\nabla B} \cdot (\mathbf{M}^{\nabla B})^{\mathrm{T}}$ used by *Shi et al.* [2005]. Unfortunately, the results for the directions are somewhat sensitive to the choice of the averaging interval $t_{\mathrm{av}}$ used for the matrix $\mathbf{M}^{\nabla B}$ ($=\nabla \boldsymbol{B}$). Table 1 shows that analysis interval $t = 350$ to 700s along with the averaging interval $t_{\mathrm{av}} = -9 \pm 500$ s (Case 21 in Table 1) can lead to fairly large errors (~15°) in the directions. In this case, however, the eigenvector directions were not completely steady over the interval $t = 350$ to 700s (not shown). For the smaller averaging interval $t_{\mathrm{av}} = -9 \pm 100$ s, these eigenvector directions were steady (Figures 7b–7d). We find the best results for the averaging interval including just the central peak in the largest eigenvalue ($\lambda_{\text{G-max}}$), and this is what we recommend to be used for this kind of analysis. This interval is about $t_{\mathrm{av}} = -9 \pm 50$ s in Figures 5 and 7. Once an averaging interval is chosen, time intervals can be chosen for which an eigenvalue is separated from the other values and for which the eigenvector direction is roughly constant. For the MHD simulation analyzed here, this prescription yields good results for the gradient directions.

[39] If we used the same averaging interval ($\langle\cdot\rangle_0$) as is used for determining the directions ($\langle\cdot\rangle$), our analysis would determine the true variance of the magnetic field gradient (section 3.2). In some sense, this would be more elegant, and would remove the apparent arbitrary choice of averaging interval. There are two reasons why we don't do this. First of all, intervals for data analysis (determining the directions) need to be chosen for which there is a good separation of the eigenvalues and for which the eigenvector directions are relatively stable. Unfortunately, the stability of the directions varies depending on the choice of averaging interval. So we cannot know in advance what are good intervals for data analysis (determining the directions) until the averaging interval is chosen. Secondly, we find that we get good results using the central region (current sheet crossing) for the averaging interval. Case 26 in Table 1 shows the results for the directions if, with a calibration error of 0.1 nT, we use the same interval $t = 350$ to 700s for the averaging and data analysis. The errors in the directions are 14° for the maximum and intermediate gradient directions, and 7.3° for the minimum gradient direction. In this case, there is significant variation in the eigenvector directions over the entire time interval. If we use $t = 350$ to 700s for the averaging interval, and $t = 590$ to 630s (over which the eigenvector directions are stable) for determining the directions (Case 27 and Table 1), we find a lower error for the maximum gradient direction, 3.2°, but a larger error, ~22°, for the intermediate and minimum gradient directions. Clearly, we found better results using the central time interval for the averaging (Case 16 in Table 1).

[40] Why is this? We needed the interval $t = 350$ to 700s to get the intermediate and minimum gradient directions (Case 16). Clearly, these components of the gradient were important within this interval. It seems that using that same time interval for the averaging removes too much information about these gradients. In other words, a strict variance (resulting from use of the same time interval) is not good enough to determine the intermediate and minimum gradient directions if the calibration errors are as large as we have used here (0.1 nT). Further tests of the method should be done to see if our prescription for choosing the averaging interval will work in general. The results for the structure velocity are not as sensitive to the averaging interval (Table 2, Cases 10–15).

[41] Further tests should also be done with other kinds of simulations, e.g., hybrid and full particle, for different reconnection configurations (i.e., the magnetopause), and with time-dependent data. As a first step in testing methods for determining the reconnection orientation and velocities, we used a time-independent snapshot of the simulation. For the actual simulation run for this study and illustrated in Figure 1, the time interval of the entire simulation was only 80s, showing that the assumption of stationary that we used would not be valid. This might indicate that shorter time intervals would need to be used for the analysis (for instance, a subset of the time interval used for Figure 6). Certainly it would indicate that the results for directions and velocity might not be as steady as we found in this paper (e.g., the almost constant velocity in Figure 9). On the other hand, a real reconnection region might be driven with a greater supply of incoming flux such that the reconnection is steady for a longer period of time than in this simulation. Or the structure velocity relative to the spacecraft might be greater. At any rate, time dependence is likely to affect the results.

[42] Our results suggest that use of $\delta\nabla \boldsymbol{B}$ can allow the gradient directions and velocities to be determined even if the calibration errors are large. Comparison of the results using both $\nabla \boldsymbol{B}$ and $\delta\nabla \boldsymbol{B}$ should also be useful in determining whether or not calibration errors are a serious problem.

[43] **Acknowledgments.** R.E.D. was supported primarily by NASA grant NNX08AV81G (MMS Theory Program) and to a lesser extent by

NSF grant ATM-0120950 (Center for Integrated Space Weather Modeling (CISM), funded by the NSF Science and Technology Centers Programs). J.B. acknowledges NASA support through the MMS and Solar-Heliophysics Theory programs.

[44] Philippa Browning thanks Goetz Paschmann and another reviewer for their assistance in evaluating this paper.

## References

Birn, J., and M. Hesse (2009), Reconnection in substorms and solar flares: Analogies and differences, *Ann. Geophys.*, *27*, 1067–1078.

Georgescu, E., et al. (2006), *Use of EDI time-of-flight data for FGM calibration check on Cluster*, *ESA SP-598*, Proc. Cluster and Double Star Symp., Noordwijk, Netherlands.

Shen, C., X. Li, M. Dunlop, Z. X. Liu, A. Balogh, D. N. Baker, M. Hapgood, and X. Wang (2003), Analyses on the geometrical structure of magnetic field in the current sheet based on cluster measurements, *J. Geophys. Res.*, *108*(A5), 1168, doi:10.1029/2002JA009612.

Shen, C., X. Li, M. Dunlop, Q. Q. Shi, Z. X. Liu, E. Lucek, and Z. Q. Chen (2007a), Magnetic field rotation analysis and the applications, *J. Geophys. Res.*, *112*, A06211, doi:10.1029/2005JA011584.

Shen, C., M. Dunlop, X. Li, Z. X. Liu, A. Balogh, T. L. Zhang, C. M. Carr, Q. Q. Shi, and Z. Q. Chen (2007b), New approach for determining the normal of the bow shock based on Cluster four-point magnetic field measurements, *J. Geophys. Res.*, *112*, A03201, doi:10.1029/2006JA011699.

Shi, Q. Q., C. Shen, Z. Y. Pu, M. W. Dunlop, Q. G. Zong, H. Zhang, C. J. Xiao, Z. X. Liu, and A. Balogh (2005), Dimensional analysis of observed structures using multipoint magnetic field measurements: Application to Cluster, *Geophys. Res. Lett.*, *32*, L12105, doi:10.1029/2005GL022454.

Shi, Q. Q., C. Shen, M. W. Dunlop, Z. Y. Pu, Q. G. Zong, Z. X. Liu, E. Lucek, and A. Balogh (2006), Motion of observed structures calculated from multipoint magnetic field measurements: Application to Cluster, *Geophys. Res. Lett.*, *33*, L08109, doi:10.1029/2005GL025073.

Sonnerup, B. U. Ö., and H. Hasegawa (2005), Orientation and motion of two-dimensional structures in a space plasma, *J. Geophys. Res.*, *110*, A06208, doi:10.1029/2004JA010853.

Sonnerup, B. U. Ö., S. Haaland, G. Paschmann, M. W. Dunlop, H. Reme, and A. Balogh (2006), Orientation and motion of a plasma discontinuity from single-spacecraft measurements: Generic residue analysis of Cluster data, *J. Geophys. Res.*, *111*, A05203, doi:10.1029/2005JA011538.

W. Baumjohann, Space Research Institute, Austrian Academy of Sciences, Schmiedlstr. 6, 8042 Graz, Austria. (baumjohann@oeaw.ac.at)

J. Birn, Los Alamos National Lab, MS D466, PO Box 1663, Los Alamos, NM 87545-0000, USA. (jbirn@lanl.gov)

R. E. Denton, Department of Physics and Astronomy, Dartmouth College, Hanover, NH 03755, USA. (richard.e.denton@dartmouth.edu)

J. F. Drake and M. Swisdak, Institute for Research and Electronics and Applied Physics, University of Maryland, College Park, MD 20742-0000, USA. (drake@umd.edu; swisdak@umd.edu)

M. Hesse, NASA Goddard Space Flight Center, Code 674, Greenbelt, MD 20771, USA. (michael.hesse@nasa.gov)

B. U. Ö. Sonnerup, Thayer School of Engineering, Dartmouth College, Hanover, NH 03755, USA. (bengt.u.o.sonnerup@dartmouth.edu)

W.-L. Teh, Laboratory for Atmospheric and Space Physics, University of Colorado at Boulder, 1234 Innovation Dr., Boulder, CO 80303-7814, USA. (teh@lasp.Colorado.Edu)